A new 3-D multi-fluid model with the application in bubble dynamics using the adaptive mesh refinement

Zhao-Li Tian[a], A-Man Zhang[a,*], Yun-Long Liu[a], Longbin Tao[b]

[a] *College of Shipbuilding Engineering, Harbin Engineering University, Harbin 150001, China*
[b] *Department of Naval Architecture, Ocean & Marine Engineering, University of Strathclyde, Glasgow, United Kingdom*

Abstract

Violent pulsating bubbles behave diversely in different circumstances. It is a multi-scale problem in both space and time. In 3-D problems, the numerical simulation is usually too expensive to implement in practice with a fixed grid. In this paper, a 3-D multi-fluid model is established based on the Eulerian finite element method and the adaptive mesh refinement technique to investigate the bubble evolution and its toroidal motion near a solid vertical wall. The mixture formula for compressible multi-fluid flow is adopted to ensure conservativeness. By means of the block-based adaptive mesh refinement, the accuracy and the efficiency of the simulation are well balanced. The present model is validated by comparing the results with an underwater explosion experiment and the existing numerical results. The results agree well and a fast convergence is observed. Then, several cases with different buoyancy parameters are simulated, and the toroidal bubble motion and their pressure load on the solid wall are analyzed. The bubble's motion exhibits complex physics, such as the formation of the crescent-shaped bubble, the air cushion effect during the jet penetration, and the nonlinear relationship between the jet impact pressure and the angle between the jet and the opposite bubble surface.

Keywords: Bubble dynamics, adaptive mesh refinement, Eulerian finite-element method, jet impact, toroidal bubble

*Corresponding author
Email address: zhangaman@hrbeu.edu.cn (A-Man Zhang)

1. Introduction

The bubble dynamics has always been a significant aspect in the research of the fluid dynamics because of its various applications, such as in underwater explosion [1, 12, 14, 20, 44, 46], sea resources exploration [10, 23, 52], biology [15], cavitation erosion and surface cleaning [5, 6, 8]. It is a typical multi-scale, transient, and nonlinear problem with the large deformation of the multi-fluid interface. The complexity of the bubble motion will be further increased if a nearby structure is presented. The boundary of the structure is usually assumed to be solid if it is rigid enough, such as the copper propeller blade to a cavitation bubble or the concrete dam to an underwater explosion bubble.

As one of the pioneers in the field of bubble dynamics research, Rayleigh [37] proposed the first practical equation describing the collapse of a spherical cavitation bubble in a free and perfect fluid field. Subsequently, a lot of past work [35, 36] contributed to improving the equation by including the other factors, such as the compressibility of the surrounding fluid, heat conduction, viscosity, and surface tension. However, researchers soon realized that the collapsing bubble did not maintain spherical due to the surface instability. Kornfeld and Suvorov [22] suggested that the non-spherical motion of a collapsing bubble might produce a much higher pressure than a spherical one on a nearby solid boundary. Naude [32] theoretically and experimentally validated this suggestion and found that the solid wall would contract the collapsing bubble to develop a high-speed jet. The bubble dynamics near a wall with different geometric shapes and material properties have renewed interest in the subject. Brujan et al. [7], Cui et al. [13]also implemented the experiments to study the interaction between a pulsating bubble and two solid joint walls. Their results show that the two walls compete to dominate the jet development, and complex evolution features are observed. Chahine et al. [9] employed both experimental and numerical fluid-structure interaction methods to investigate the cavitation bubble collapse near a solid wall with polymetric coating and found that the material property of the coating layer had a significant influence on the jet development and the impact pressure.

Among the many numerical computational fluid dynamics methods, the Boundary Element Method (BEM) [5, 20, 21, 44, 50] is one of the numerical methods that are first successfully used in the non-spherical bubble dynamics simulation because it reduces the spatial dimensions by 1. This was a significant advantage over the other domain-mesh methods in the late 20th century when the computational resources were minimal. It is the boundary that needs to be discretized instead of the whole flow domain. Besides, the far-field condition is automatically satisfied such that the truncation error of the computational domain is avoided. Many researchers

contributed to this field and made significant progress in the non-spherical bubble dynamics simulation. Blake et al. [5] established an axisymmetrical model based on BEM to investigate a cavitation bubble collapsing nearby a solid wall. Wang et al. [45] extended the simulation to the toroidal bubble generated by the jet penetration by introducing a vortex ring inside the bubble. This approach resolves the conflict between the potential theory used in BEM and the velocity circulation around the toroidal bubble. When the solid wall's normal does not align with the gravity, the problem is no longer axisymmetrical. Thus, Wang [44] employed a 3-D numerical model based on the BEM to investigate the jet development subject to the combined effects of an inclined wall and the buoyancy. However, the toroidal stage of the bubble is not included in this paper. Thus, Klaseboer et al. [20] combined the 3-D BEM and the vortex ring model and simulated an underwater explosion bubble interacting with a vertical wall. Their results of the impact pressure were compared and agreed with the experimental results well. Furthermore, Zhang and Liu [50] improved the 3-D bubble dynamics model based on the BEM to capture more deformation details of the toroidal bubble, and it was adopted in Liu et al. [28] where the influence of the free surface was included in the interaction between a bubble and the nearby solid wall. It was found that the toroidal bubble might further break into two toroidal [51] or a crescent-shape [28] bubble. Because of the requirement of complex mesh manipulations for bubble split and merge, introducing and removing vortex rings, it is non-trivial to implement in the 3-D BEMs.

The domain-mesh methods for computational fluid dynamics have developed rapidly along with the growth of computational power. However, the interface treatments require special attention because the interface is usually not coincident with the cell boundaries. In the cut-cell method [48], the interface cell cut by the moving interface and the irregular subcells are solved as normal cells. However, explicit tracking of the interface is required, and special manipulations should be included to avoid small and narrow subcells. With a proper implicit interface capture method, e.g., the level-set method [16, 24, 42], the volume of fluid (VOF) method [17, 38, 49], or the γ-based method [11], the complex topology change of the collapsing bubble requires no special treatments and is no longer a difficulty. Besides, suppose the Euler equation describes the fluid flow and discretized in the numerical model. In that case, the fluid's compressibility is naturally considered while it is non-trivial in the BEMs. One significant challenge in these implicit interface capture methods is the conservativeness issue. The level-set method coupled with the ghost fluid method proposed by Fedkiw et al. [16] solves two single-medium problems with properly defined ghost cell states in which the conservativeness is not enforced. A lot of efforts have been made to improve the conservativeness within the framework of the level-set method and

the ghost fluid method [27, 41]. By contrast, the conservation in the mixture formula [31, 38] is trivial although a transition layer of several cells is required to represent the interface. Johnsen and Colonius [19] employed the quasi-conservative interface capturing formula to investigate the non-spherical bubble collapse beside a solid wall induced by a strong shock. Tian et al. [40] established an axisymmetric model based on the Eulerian finite element method(Eulerian FEM) [3] and investigated the jet development of an underwater explosion bubble and its impact on a solid horizontal wall. Another difficulty in the pulsating bubble simulation is that the computation is expensive if the compressibility of the surrounding fluid is considered. A large number of time increments are required due to the Courant–Friedrichs–Lewy(CFL) condition.

When it comes to a fully 3-D simulation, the unknown degrees of freedom (DOF) in the domain-mesh methods dramatically increases to an impractical level, especially in the multi-scale bubble pulsating problem. Thus, an Adaptive Mesh Refinement (AMR) technique is essential to reduce the DOFs by coarsening the local mesh where the solution is not important and has little influence on the global solution. The patch-based AMR first introduced by Berger and Colella [4] proposed have been widely used in CFD codes, such as the BoxLib, AMROC, and Chombo. In 3-D block-based AMR, a set of non-overlapping boxes is find to cover the region requiring refinement. These boxes have meshed with higher resolution than the base mesh. The results calculated with the coarser mesh is mapping to the finer one to provide it a ghost boundary, while the results obtained in the finer mesh with this boundary is projected back to the coarse one. Another approach to the AMR is the block-based AMR [30, 34], in which each block is a box with the same data structure, and they are refined based on the oct-tree algorithm. One or more layers of guardcells are attached to each block's outside boundary, and their data is copied from the adjacent blocks for communication.

In the present paper, the Eulerian FEM is adopted to resolve the motion of a pulsating bubble. We use the block-based AMR implemented with the open-source package Paramesh [30, 34] such that the efficiency and accuracy can be balanced in simulating the bubble pulsation and toroidal motion. The rest of the present paper is organized as follows. In section 2, the underlying theory and numerical techniques are presented relating to the Eulerian FEM and the AMR implementation. Then, the numerical model is validated by comparing it with an underwater explosion experiment in section 3. In section 4, several cases of a high-pressure bubble moving beside a vertical wall are simulated and analyzed with the present model. The results are also compared with the BEM to verify the accuracy. At last, some conclusions are drawn in section 5.

2. Theoretical and Numerical Models

2.1. Problem description and basic equations

In this paper, the bubble dynamics near a vertical wall is concerned. The bubble is initially placed in the still water at a depth of h with a higher pressure of the internal gas than that of the ambient water. A solid vertical wall is located with a distance of d from the center of the initial bubble. This problem is abstracted from the underwater explosion bubble near a submerged structure or a vertical dam and has been studied both experimentally and numerically. The detonation process is usually much shorter than the bubble motion. Thus, it is reasonable to assume that the fluid flow is initially at rest. The internal gas and the surrounding liquid forms a multi-fluid Riemann problem because of the pressure difference across the bubble interface. Then, the bubble starts expanding, with the contact discontinuity moving outwards. If the solid wall is absent, the bubble's motion can be roughly described by the Rayleigh-Plesset equation, and a multi-cycle pulsation will occur.

In the pulsating bubble problems, the multi-fluid interface usually experiences great deformation. For example, the maximum radius of an underwater explosion bubble can be as large as dozens of times of the initial one such that the conservative error is amplified significantly. Thus, the mixture formula for the multi-fluid problem is adopted for its natural advantages in conservativeness. Assuming that all the fluid components share a single pressure within a cell, the Euler equations with the mixture formula [38] for the multi-fluid system are

$$\begin{cases} \dfrac{\partial \alpha_i}{\partial t} + \nabla \cdot (\alpha_i \mathbf{u}) = \alpha_i \dfrac{\bar{\kappa}}{\kappa_i} \nabla \cdot \mathbf{u}, \\ \dfrac{\partial (\alpha_i \rho_i)}{\partial t} + \nabla \cdot (\alpha_i \rho_i \mathbf{u}) = 0, \\ \dfrac{\partial (\bar{\rho} \mathbf{u})}{\partial t} + \nabla \cdot (\bar{\rho} \mathbf{u} \otimes \mathbf{u}) + \nabla p = \bar{\rho} \mathbf{g}, \\ \dfrac{\partial (\alpha_i \rho_i e_i)}{\partial t} + \nabla \cdot (\alpha_i \rho_i e_i \mathbf{u}) + \alpha_i \dfrac{\bar{\kappa}}{\kappa_i} p \nabla \cdot \mathbf{u} = 0 \end{cases} \tag{1}$$

where α is the volume fraction bounded by 0 and 1, ρ is the mass density, $\mathbf{u} = (u_1, u_2, u_3)$ is the material velocity, e represents the specific internal energy per unit mass, $\kappa = \rho c^2$ is the bulk module of fluid with c representing the sound speed, and $\mathbf{g}$ is gravity. The subscript i indicates a variable of the fluid i, $\otimes$ is the tensor product operator, and the bar over a variable represents an average quantity of the mixture fluid. The factor of $\alpha_i \frac{\bar{\kappa}}{\kappa_i}$ in the first and fourth equations is included to consider the compressibility difference of the fluid components in the mixture. Note that only α_1 is required to be solved and α_2 is then recovered with the fact that $\alpha_1 + \alpha_2 = 1$.

For the fluid mixed by fluid 1 and fluid 2, the average density and bulk module are determined by

$$\bar{\rho} = \alpha_1\rho_1 + \alpha_2\rho_2, \tag{2}$$

and

$$\bar{\kappa} = \frac{\kappa_1\kappa_2}{\alpha_1\kappa_2 + \alpha_2\kappa_1} \tag{3}$$

with the assumption that the two fluids share the same pressure. Besides, the sound speed of the mixture can be recovered by the relationship of

$$\bar{\kappa} = \bar{\rho}\bar{c}^2, \tag{4}$$

which can be used for any equation of state (EoS) with an explicitly written sound speed.

For compressible fluids, the EoS of each fluid is required to close the Euler equations. In this paper, the Tammann EoS [18] is chosen to model the surrounding water of the bubble in the following form:

$$p = \rho e(\gamma - 1) - \gamma P_w, \tag{5}$$

with the sound speed given by

$$c^2 = \frac{p + P_w}{\rho}\gamma, \tag{6}$$

where γ and P_w are constants that taken as 7.15 and 330.9MPa. When P_w is 0, Eq. (5) degrades to the ideal gas EoS:

$$p = \rho e(\gamma - 1), \tag{7}$$

which is used to model the internal gas of the bubble with $\gamma = 1.25$ [20, 50].

2.2. Eulerian FEM with operator split

The Eulerian FEM [25, 26, 40] is used to solve Eq. (1) to investigate the dynamics of a bubble beside a vertical solid wall. Firstly, we rewrite Eq. (1) in the vector form

$$\frac{\partial \mathbf{E}}{\partial t} + \mathbf{u}\cdot\nabla\mathbf{E} + \mathbf{E}\nabla\cdot\mathbf{u} = \mathbf{S}, \tag{8}$$

where the vectors $\mathbf{E}$ and $\mathbf{S}$ are given by

$$\mathbf{E} = \begin{bmatrix} \alpha_i \\ \alpha_i\rho_i \\ \bar{\rho}\mathbf{u} \\ \alpha_i\rho_i e_i \end{bmatrix}, \mathbf{S} = \begin{bmatrix} \alpha_i\frac{\bar{\kappa}}{\kappa_i}\nabla\cdot\mathbf{u} \\ 0 \\ \bar{\rho}\mathbf{g} - \nabla p \\ -\alpha_i\frac{\bar{\kappa}}{\kappa_i}p\nabla\cdot\mathbf{u} \end{bmatrix}.$$

Then, the operator split technique is employed to split Eq. (8) into

$$\frac{\mathrm{d}\mathbf{E}}{\mathrm{d}t} + \mathbf{E}(\nabla \cdot \mathbf{u}) = \mathbf{S}, \tag{9}$$

and

$$\frac{\partial \mathbf{E}}{\partial t} = \frac{\mathrm{d}\mathbf{E}}{\mathrm{d}t} - \mathbf{u} \cdot (\nabla \mathbf{E}). \tag{10}$$

Eq. (9) is based on the Lagrangian perspective, and the material moves along with the mesh. Thus, we can apply the traditional explicit FEM to Eq. (9) [47]. Then, Eq. (10) is solved by remapping the conservative vector $\mathbf{E}$ from the deformed mesh to the original mesh. The solvings of these two equations are referred to as the Lagrangian step and the Eulerian step, respectively. The operator split technique makes the combined method stable and robust, especially for the violent bubble motion with a great density ratio across the interface. Typically, it has the second order of accuracy in space and the first order of accuracy in time.

In the following subsections, the detailed formulas and numerical techniques in these two steps are explained.

2.2.1. Lagrangian step

In the Lagrangian step, the mesh is assumed to move with the fluid material. In this paper, the momentum equation in the Lagrangian step is solved only once for both of the two fluid components with the mixture fluid technique and the explicit FEM [3, 47]. Pluging the conserving equation of mass into the conserving equation of momentum in Eq. (9), we can obtain

$$\bar{\rho}\frac{\mathrm{d}\mathbf{u}}{\mathrm{d}t} = \bar{\rho}\mathbf{g} - \nabla p. \tag{11}$$

Let's discretize the computational domain into cells, and denote Φ_P as the shape function for node P. Then we can express the solution by $\mathbf{u} = \Phi_Q \mathbf{u}^Q$. Herein, the superscript Q indicate the nodal variable at node Q, and the Einstein summation convention is used. Multiply Eq. (11) by the shape function Φ_P and integrate it over the computational domain Ω, we can derive the semi–discretized form of Eq. (11) as

$$\int_\Omega \Phi_P \Phi_Q \bar{\rho}\,\mathrm{d}V\,\frac{\mathrm{d}\mathbf{u}^Q}{\mathrm{d}t} = -\int_{\partial\Omega} p\hat{\mathbf{n}}\Phi_P\,\mathrm{d}S + \int_\Omega (\bar{\rho}\mathbf{g}\Phi_P + p\nabla\Phi_P)\,\mathrm{d}V, \tag{12}$$

where $\partial\Omega$ is the boundary of Ω, and $\hat{\mathbf{n}}$ is its outward-pointing unit vector. We can rewrite Eq. (12) in the matrix form:

$$\mathbf{MA} = \mathbf{F}, \tag{13}$$

where $\mathbf{M} = \left[\int_\Omega \Phi_P \Phi_Q \bar{\rho}\, \mathrm{d}v\right]$ is the mass matrix, $\mathbf{A} = \left[\frac{\mathrm{d}\mathbf{u}^Q}{\mathrm{d}t}\right]$ is the nodal acceleration matrix, $\mathbf{F}$ is the matrix of nodal force corresponding to the right-hand side of Eq. (12).

With the newly calculated acceleration, we advance the nodal velocity and displacement explicitly. After that, the other conservative quantities are updated with corresponding equations extracted from Eq. (9):

$$\frac{\mathrm{d}\alpha_i}{\mathrm{d}t} = \alpha_i \left(\frac{\bar{\kappa}}{\kappa_i} - 1\right) \nabla \cdot \mathbf{u}, \tag{14}$$

$$\frac{\mathrm{d}\rho_i}{\mathrm{d}t} = -\rho_i \frac{\bar{\kappa}}{\kappa_i} \nabla \cdot \mathbf{u}, \tag{15}$$

and

$$\frac{\mathrm{d}(\rho_i e_i)}{\mathrm{d}t} = -(p + \rho_i e_i) \frac{\bar{\kappa}}{\kappa_i} \nabla \cdot \mathbf{u}. \tag{16}$$

The time increment in this paper is calculated with

$$\Delta t = \mathrm{CFL} \left[\min\left(\frac{L_e}{\bar{c} + |\mathbf{u}|}, |\nabla \cdot \mathbf{u}|^{-1}\right)\right]^{\min}, \tag{17}$$

where L_e is the minimal length dimension of the element, CFL is a constant scale factor which is taken as 0.5 in this paper, and the superscript "min" means the minimum value over all the elements in the computational domain. The second part in the min operator is used to prevent the negative volume during one step.

2.2.2. Eulerian step

In the operator split procedure, the fluid material and computational mesh are advanced together in the Lagrangian step for a whole time increment, following which an Eulerian step is implemented. In this step, the physical time is not advanced, and only a conservative remapping procedure is performed by calculating the advection between adjacent cells with the following steps:

(1) Reconstruct medium interface in multi-fluid cells using the PLIC(Piecewise Linear Interface Construction) algorithm [3, 49]:
By denoting the coordinate vector $\mathbf{x} = (x, y)$, the linear interface can be expressed by a plane equation

$$\mathbf{n} \cdot \mathbf{x} + b = 0. \tag{18}$$

To obtain the normal vector $\mathbf{n}$, a quadratic function $f(\mathbf{x}) = \mathbf{K} \cdot \mathbf{R}$ is constructed by fitting the volume fraction α around the current cell with the least square method [39]. Herein, $\mathbf{R}(\mathbf{x}) = [x^2, y^2, xy, x, y, 1]^T$ is a complete set of the basis

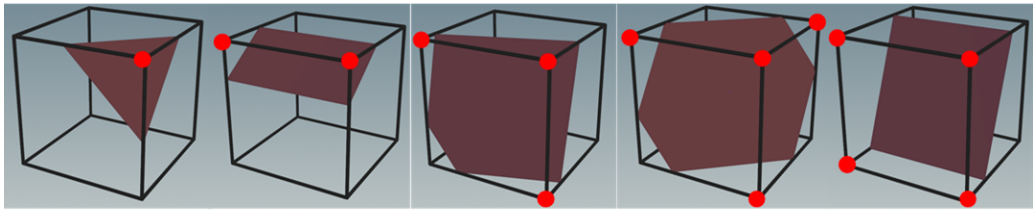

Figure 1: Basic geometry configurations for a cell cutted by a planar interface.

vector in the 3-D quadratic space. $\mathbf{K} = [k_1, k_2, k_3, k_5, k_6]^T$ is the coefficient vector obtained by solving the following linear system:

$$\mathbf{K} = \mathbf{A}^{-1} \sum_{j=1}^{27} \mathbf{R}(\mathbf{x}_j)\alpha_j \tag{19}$$

where the summation runs over the current cell and its immediate neighbors, i.e., the $3 \times 3 \times 3$ mesh block around the current cell, $\mathbf{x}_j$ is the cell center coordinate, and $\mathbf{A} = \mathbf{R} \otimes \mathbf{R}$. If a uniform mesh is used in the simulation and a dimensionless local coordinate system is established with its origin locating at the current cell center, the inverse of the matrix $\mathbf{A}$ can be calculated once and stored for the use thereafter to simplify the calculation. Then, the normal vector can be approximated by $\mathbf{n} = \frac{\nabla f}{|\nabla f|}$, and the constant b in Eq. (18) can be obtained by an iterative method with the fact that the volume of the cell cut by the interface is $\alpha \Delta x^3$.

(2) Calculate advected volume geometrically based on the velocity obtained in the Lagrangian step and the constructed interface. With proper rotating manipulation, we may encounter with the five basic geometry configurations, as shown in Fig. 1. This step is trivial, and the readers can refer to Benson [2];

(3) Advect cell-centered variables, i.e., mass and internal energy, using the MUSCL (Monotonic Upwind Scheme for Conservation Law) [3];

(4) Convect the node-centered momentum using the HIS (Half Index Shift) algorithm proposed by Benson [2]. In this paper, the MUSCL is used instead of the first-order donor-acceptor scheme to advect the 8 auxiliary cell-centered variables constructed for the 8 nodes such that the second-order accuracy is achieved.

(5) Based on the new density and internal energy, the cell pressure is calculated with the EOS and the new time increment is calculated with the sound speed. Note that a pressure equilibrium is required to eliminate the pressure difference between the two fluid components within a cell. In this paper, the internal energy

is exchanged between the two fluids with the following equations to achive the pressure equilibrium

$$(\rho e)_1 = (\rho e)_1^* - \frac{1}{\alpha_1}\Delta(\rho e) \tag{20}$$

$$(\rho e)_2 = (\rho e)_2^* + \frac{1}{\alpha_2}\Delta(\rho e), \tag{21}$$

where

$$\Delta(\rho e) = \frac{\alpha_1\alpha_2\Delta p^*}{\frac{\alpha_2\partial p_1}{\partial(\rho e)_1} + \frac{\alpha_1\partial p_2}{\partial(\rho e)_2}}.$$

Herein, the superscript * represents the values before the pressure equilibrium, $\Delta p^* = p_1^* - p_2^*$ is the pressure difference and $\frac{\partial p}{\partial(\rho e)}$ can be calculated with EoS easily.

(6) Go to the next time increment and start a new Lagrangian step.

2.3. Adaptive mesh refinement

For a fully 3-D simulation of an oscillating bubble, the AMR is essential to reduce the computational complexity to a reasonable scale. The open-source package Paramesh [29, 33] is adopted and modified in the present paper to archive the AMR because of its flexibility. The Paramesh package is a block-based AMR package that manages the mesh refinement procedure and processor communications with the Massage Passing Interface. Each block has the same data structure, allowing the users to connect the Paramesh and an existing serial and non-AMR solver with minor modifications. To simplify the demonstration, Fig.2 shows a 2-dimensional block in the Paramesh. The cells in the yellow color are the real ones to be solved

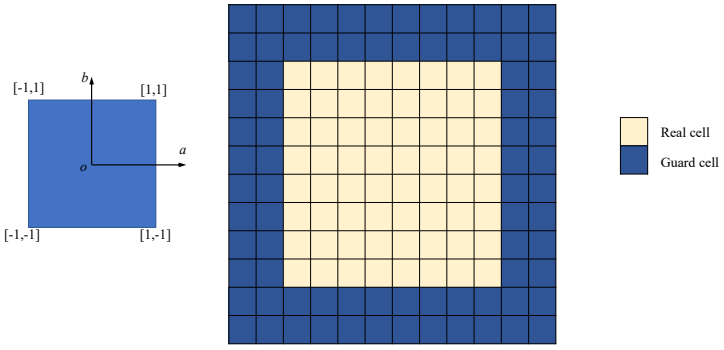

Figure 2: Guardcell structure of a 2-dimensional unified block.

with the Eulerian finite element method, while the blue cells on each edge of the block are the guardcells providing boundary conditions for the real ones. Paramesh communicates between adjacent blocks and the conservative quantities of the guardcells are interpolated from the overlaped cells of the neighbor blocks at the beginning of each time increment. In this paper, the block dimension is taken as $8 \times 8 \times 8$ and 2 additional layers of guardcells are used. As shown in Fig.3, the real cells of 2 blocks are adjac [illegible] al cells from the

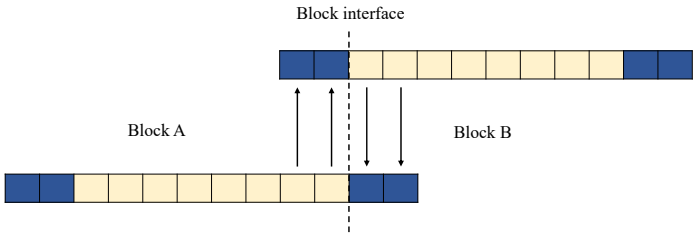

Figure 3: Sketch for the Guardcell filling procedure. The arrows indicate the direction in which the information moves.

At the beginning of each time increment, the state variables of the real cells are inherited from the previous increment. But those of the guardcells are taken from the corresponding real cells of the adjacent block. If the two blocks are in the same refinement level, the guardcell filling procedure is straightforward, as shown in Fig. 3. Otherwise, conservative restriction and prolonging procedures are required.

As shown above, in the present numerical model, the fluid velocity is a nodal vector. However, the velocity at nodes shared by different blocks could be inconsistent, which will lead to pressure fluctuation near the intersection of fine and coarse blocks. Thus, a few modifications are made as follows to fill the guardcell's nodal velocities in the Paramesh:

(1) If a block's neighbor is in the same refinement level, the velocities of the nodes on the shared face are overridden as the algebraic average of the velocities from both sides;
(2) If a block's neighbor is a finer block, the nodal velocities on the shared face are overridden as the velocities from the neighbor block;
(3) If a block's neighbor is a coarse one, the nodal velocities on the shared face remain unchanged.

With the modifications above, the nodal velocities on the shared block faces are enforced to be consistent.

By choosing proper constant parameters for the refinement, i.e., the maximum refinement level $L_{\max}$, the minimum refinement level $L_{\min}$, the pressure difference thresholds s_u and s_d, all the blocks are labeled based on the following criterion:

(1) If $(\alpha_{\max} - \alpha_{\min})$ in the current block is greater than a prescribed small constant s_c, it is labeled as an interface block and requires refinement. Herein, $\alpha_{\max}$ and $\alpha_{\min}$ are the maximum and minimum values of the volume fractions among all the fluid components in the current cell, and s_c is taken as 10^{-9};
(2) If the maximum spatial difference of the pressure p is greater than s_u, then the current block is labeled as a critical block which requires refinement;
(3) If the maximum spatial difference of p in the current block is smaller than s_d and it has no neighbor in a higher refinement level than itself, it is labeled as a block that requires de-refinement.

After the labelling process, the refinement and de-refinement are implemented iteratively such that the new refinement level is bounded by $L_{\max}$ and $L_{\min}$ and the refinement level difference between 2 adjacent blocks does not exceed 1.

2.4. Non-dimensionalization and initial conditions

It is necessary to write all the physical variables in the non-dimensional form to obtain a uniform numerical accuracy in different simulations. Following the previously published papers [20, 50] in bubble dynamics, we chose the maximum radius of the bubble R_m, the fluid density ρ_f and the static pressure at a depth of the bubble center $P_\infty = P_{atm} + \rho_f g h$ as the variable scales for the non-dimensionalization of length, density, and pressure. And the scales of the other variables can be calculated correspondingly. In Tab. 1, these quantity scales are listed together.

Table 1: Quantity scales for non-dimensionalization

Length	Pressure	Density	Velocity	Acceleration	Time
R_m	P_∞	ρ_f	$\sqrt{\frac{P_\infty}{\rho_f}}$	$\frac{P_\infty}{R_m \rho_f}$	$R_m\sqrt{\frac{\rho_f}{P_\infty}}$

With these characteristic quantities, the initial conditions of the bubble can be given non-dimensionally by the strength parameter $\epsilon = \frac{P_0}{P_\infty}$, the distance parameter $\gamma_w = \frac{d}{R_m}$ and the buoyancy parameter $\delta^2 = \frac{\rho_f g R_m}{P_\infty}$. Herein, d is the distance of the explosive charge to the solid wall.

2.5. Computational domain setup

The computational domain is taken as a hexahedron of $[0, 5R_m] \times [0, 5R_m] \times [-5R_m, 5R_m]$ as shown in Fig. 4. The initial bubble center is at $[\gamma_w R_m, 0, 0]$. The six faces of the computational domain are denoted as Faces A to F. Faces C and F are impenetrable, and all the other faces are the truncation boundaries of the computational domain. To minimize the spurious reflection of the truncation boundary, the non-reflecting boundary condition proposed by Liu et al. [25] is applied on Face A, B, D, and E. The computational domain is sized by $5R_m \times 5R_m \times 10R_m$ and consists of two base blocks. Typically, Face F represents the solid wall, and one half of the computational domain is simulated with the symmetry plane $y = 0$. However, if γ_w is set to 0, Face F turns to a symmetry plane, and the problem imitates the one-fourth fluid field of a bubble moving in the free field.

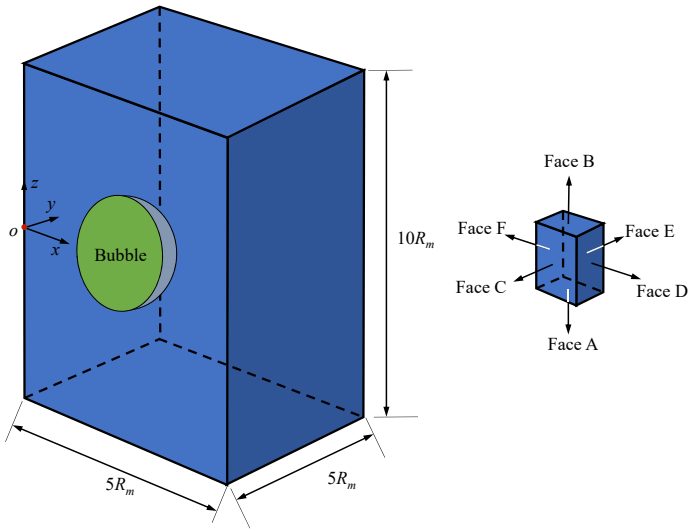

Figure 4: Configuration of the bubble motion near a vertical wall

3. Model validation with underwater explosion experiment

To validate the present numerical model, an underwater explosion experiment is carried out in a water tank sized by $4m \times 4m \times 4m$. A high-speed camera is used to capture the images of the underwater explosion process. Due to the strong shock load of the underwater explosion, it is non-trivial to set up a hard-enough boundary in an experiment when studying the interaction of an underwater explosion bubble and a nearby fixed solid wall. Thus, we use two identical explosives detonating at the same depth to mimic the situation of one underwater explosion near a solid wall. This can be justified with the mirror theory, which has been used by Wang [44] and Liu et al. [28] to investigate the bubble dynamics near a solid wall.

The two charges of 10g Hexogen explosives are placed horizontally with a distance of 0.68m and a depth of 1.85m. The maximum radius of the bubble is 0.34m, which corresponds to a case of a bubble moves beside a solid vertical wall with a buoyancy parameter $\delta = 0.0277$ and a distance parameter $\gamma_w = 1.0$. The nearest boundary is about 1.36m away from the bubble such that the boundary effect can be ignored. In the simulation, the initial conditions are taken as $\epsilon = 572$ and $\delta = 0.0277$ with the method proposed by Klaseboer et al. [20]. The lowest refinement level is set to 3, and the highest refinement level is set to 6. Thus, the finest cell size is 6.6mm and there are 102 cells across the maximum perimeter of the bubble.

The comparison of the present results and the experiment are shown in Fig. 5. It can be seen that the two sets of results agree with each other well in the sense of bubble evolution. The two bubbles expand and collapse simultaneously, which offsets the induced velocity at the x direction on the plane $x = 0$. Thus, the bubble motion is identical to that besides a solid wall of $x = 0$. During the collapsing phase, the two bubbles are attracted by each other because of the Bjerknes force. A high-pressure region emerges near each bubble, which drives it to develop a liquid jet towards the other bubble, as shown in Fig. 3(c) and (d). When $t = 66.3$ms, the two bubbles are penetrated by the liquid jets and form two toroidal bubbles.

4. Results and discussion

4.1. General features of a bubble collapsing beside a solid wall

The non-dimensionalization of the bubble dynamics shows that the buoyancy effect depends on the buoyancy parameter. Thus, a greater maximum radius is required to increase the buoyancy effects in the bubble motion. However, it is non-trivial to implement a large scale underwater explosion experiment and record the bubble's evolution. Thus, in this section, the present numerical results are compared with the BEM results presented by Wang [44]. The case shown in Fig. 16 in Wang [44] is chosen of which the initial conditions are $\epsilon = 100$, $\delta = 0.5$ and $\gamma_w = 1.0$. It should be noted that a greater initial radius of the bubble is adopted in this paper than that used in the BEM. The reason is that the present model takes the compressibility of the surrounding fluid into account so that the energy dissipation through the pressure waves is included. To archive the same maximum radius of 1, the initial radius must be greater. It was obtained by backward integrating the Rayleigh-Plesset equation from the maximum radius [43]. However, because the Rayleigh-Plesset equation does

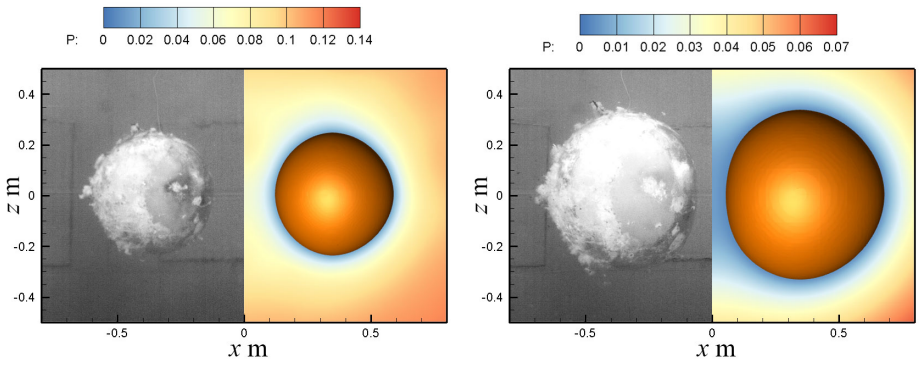

(a) $t = 7.0$ms

(b) $t = 24.8$ms

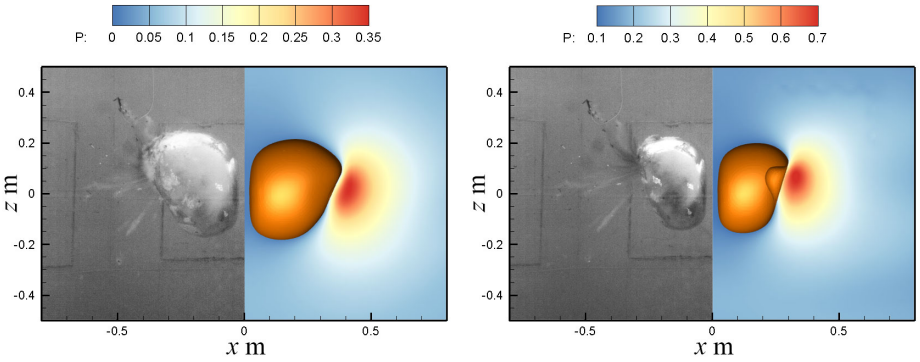

(c) $t = 58.1$ms

(d) $t = 63.0$ms

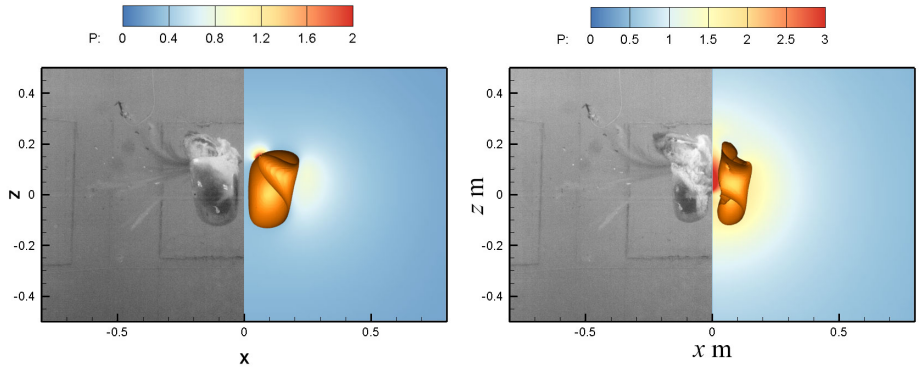

(e) $t = 66.3$ms

(f) $t = 70.1$ms

Figure 5: Comparison of the simulated results(right) and the experiment(left) for the underwater explosion bubbles generated by 2 10g Hexogen charges at the depth of 1.85m and a distance of 0.84m away from each other. The color contour represents the pressure field with the unit of MPa.

not consider the discontinuous shock at the beginning of the expansion, it can only give a set of initial conditions that the bubble is initially expanding at a certain velocity, which is not applicable in this paper. Thus, we take several simulations with the 1-dimensional Eulerian FEM to obtain the proper initial radius iteratively, and $R_0 = 0.2$ is used in the following simulations. In this case, buoyancy plays an important role in the evolution of the bubble because of the great buoyancy parameter δ. It corresponds to an underwater explosion bubble with $R_m = 20$m at $h = 40$m if the gravity acceleration is approximated by 10m/s^2. Although it is not quite practical for such a great bubble, we chose this case because the buoyancy effect is comparable to that of the solid wall, which leads to a complex evolution behavior of the bubble.

4.2. Comparison with BEM results and convergence test

As shown in Wang [44], the bubble will collapse after it reaches its maximum volume, and a jet will develop under the combined effect of the solid wall and buoyancy. In Fig.6, the fluid fields on the xoz plane at $t = 0.976, 1.873$, and 2.207 are shown with the color contours represent the pressure field, and the solid black curves indicate the bubble profiles. The maximum refinement level $L_{\max}$ is taken as 6 here. With the parallelization accomplished with the MPI(Massage Passing Interface), the simulation takes 16 hours on a desktop with an Intel I7-9700 (4 threads are used here) CPU and 32Gb RAM.

It can be seen that a high-pressure region forms beneath the bubble which drives it to develop an inward jet. Because of the existence of the solid wall, the high-pressure region deviates to the right side which deflects the jet towards the wall. The profiles at the same time are extracted from Wang [44] and plotted as red crosses in Fig. 6 for comparison. The results agree well with each other, which validates the present model.

To demonstrate the convergence of the present model, Fig. 7 compares the bubble profiles at $t = 2.207$ on the xoz plane simulated with the maximum refinement level $L_{\max} = 6$, 5, and 4, respectively. It shows that the result is poor with $L_{\max} = 4$, where the finest cell size is about 0.078 and is relatively coarse compared with the initial radius $R_0 = 0.2$. With $L_{\max}$ increased to 5, the results are improved significantly, and the bubble profile is very close to that with $L_{\max} = 6$, which indicates that the present model converges quickly with the increase of $L_{\max}$.

4.3. Crescent-shaped bubble after jet penetration

With the present model, we further simulate the bubble motion after the jet penetration, as shown in Fig.8. We can see that after the bubble reaches its maximum

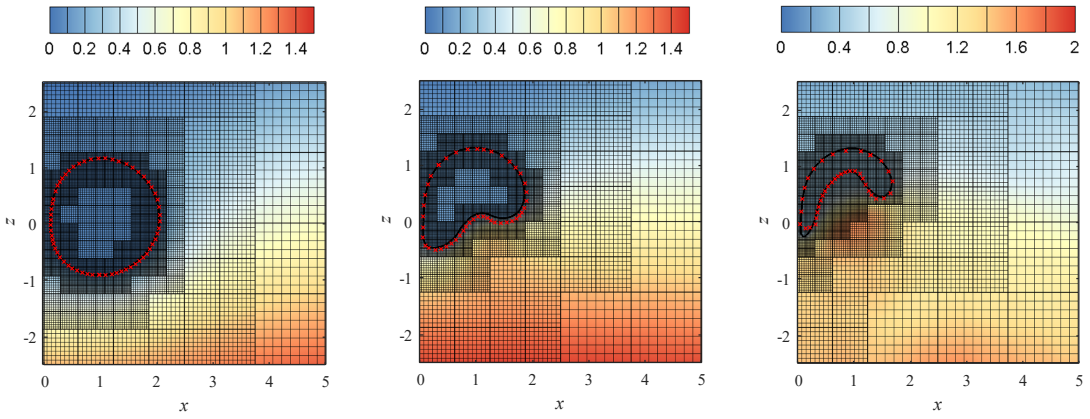

(a) $t = 0.976$ (b) $t = 1.873$ (c) $t = 2.207$

Figure 6: Comparison of bubble profile on xoz plane from present model(black curves) and Wang [44](red crosses) for a bubble collapsing besides a vertical wall(plane $x = 0$). The color contour represents the pressure field. The thick grid lines show the boundaries of blocks and the thin grid lines indicate the cells.

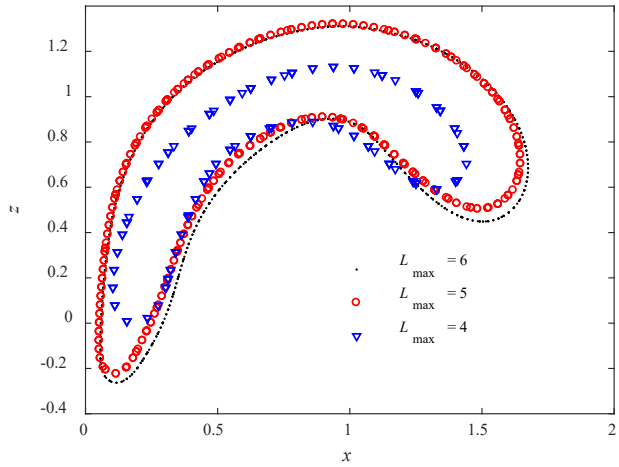

Figure 7: Comparison of bubble profiles at $t = 2.207$ on the xoz plane with maximum refinement level $L_{\max} = 6$, 5 and 4, respectively.

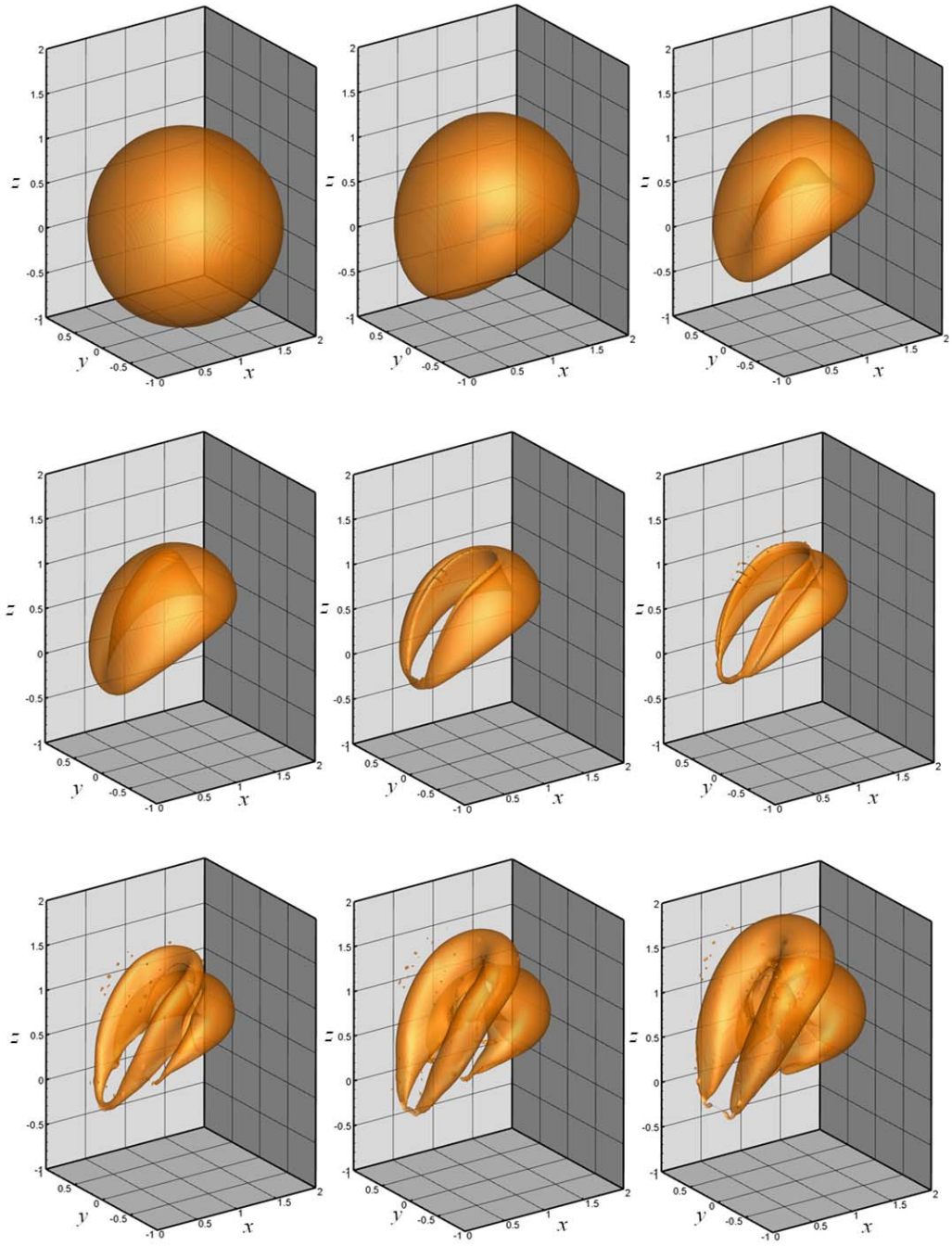

Figure 8: Collapse of a bubble beside a solid wall(plane $x = 0$) with $\epsilon = 100, \gamma_w = 1.0$. For the first row $t = 0.976$, 1.873 and 2.207, respectively. For the second row, $t = 2.386$, 2.453 and 2.541, respectively. For the third row, $t = 2.698$, 2.839 and 3.006, respectively.

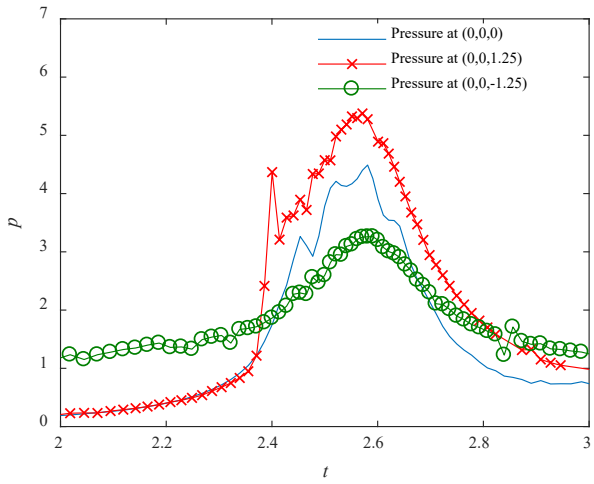

Figure 9: Bubble impact pressure curves on the solid wall at (0,0,0), (0,0,1.25) and (0,0,-1.25).

volume at $t = 0.976$, a wide jet develops from the bottom of the bubble due to the combined effects of the buoyancy and Bjerkeness force caused by the solid wall. The jet is wide in the y direction while thin in the x direction. At $t = 2.386$, the jet penetrates the bubble at its inclined top close to the solid wall and turns the bubble into toroidal shape. It should be noted that the lower part of the inclined toroidal bubble is much thinner than the rest due to the bias of the jet. With the bubble continue collapse, a new toroidal bubble develops upward from the vortex eye due to the upward velocity of the water jet. These two toroidal bubbles connect, and the internal gas is transported from the old (lower) one to the new (upper) one. Their total volume reaches the minimum value at $t = 2.541$ and starts rebounding. Then, both bubbles break at the thinnest parts and turn crescent-shaped, which has seldom been investigated before. It is non-trivial to simulate the jet penetration, break into two toroidal bubbles, and further break into two crescent-shaped bubbles with the BEMs, requiring complex manipulations, such as the surface remesh, vortex ring placement, and removal.

Fig.9 shows the pressure histories at three locations on the solid wall. At $\mathbf{p}_1 = (0, 0, 0)$ and $\mathbf{p}_3 = (0,0,-1.25)$, the pressure curves are relatively smooth and no obvious jet impact pressure is observed. By contrary, a sharp increase can be seen on the pressure history curve at $\mathbf{p}_2 = (0, 0, 1.25)$ when the jet penetrates the bubble as shown in Fig.9(d). The reason is that the jet impact pressure mostly propagates in the jet's direction, and the points $\mathbf{p}_1$ and $\mathbf{p}_3$ are not in the impact region. Usually, the abrupt change of flow domain topology would lead to impact pressure in the

surrounding flow. However, only a weak fluctuation can be seen from the pressure history of point $\mathbf{p}_3$. The reason can be attributed to the circular velocity. Based on the vortex ring theory of a toroidal bubble [45], the velocity circulation around every toroid section should be the same and keep constant as long as the topology of the flow domain remains unchanged. Theoretically, it should be proportional to the inverse of the cross-section perimeter. If the size of the cross-section varies along the toroid circle, the circular velocity around the thinnest section can be as high as infinity before it breaks, which leads to a great centrifugal force of the fluid slowing the impact process so that the toroidal bubble breaks smoothly.

4.4. Evolution of inclined toroidal bubble with different buoyancy parameters

Based on the previous section, the buoyancy parameter δ is changed to 0.25 and 0.1, respectively, which are more practical for the corresponding engineering cases. The other initial conditions and the computational setup remain the same. In Fig. 10, the pressure field around the bubbles which drive them to develop the liquid jets are shown by iso-pressure surfaces, and the bubble are shown with the green surfaces. We can see that with the increase of the buoyancy parameter from

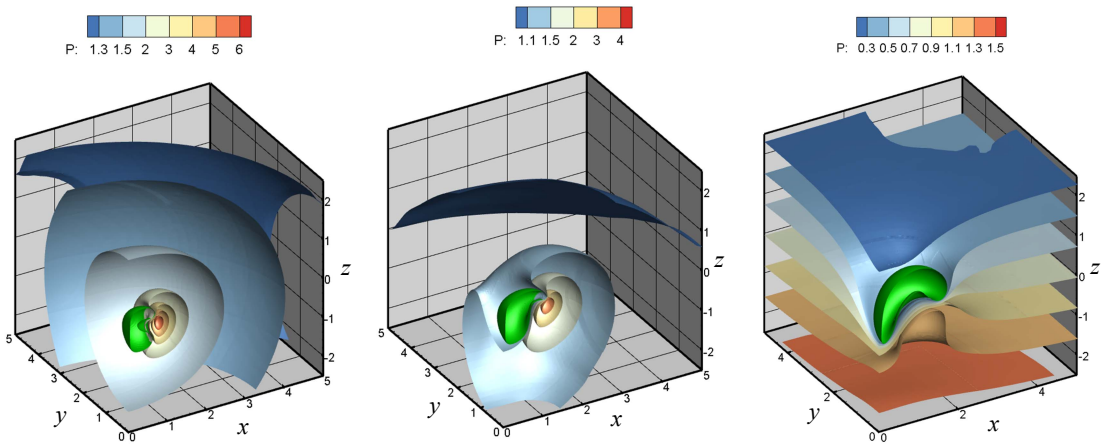

(a) $\delta = 0.1, t = 2.351$ (b) $\delta = 0.25, t = 2.248$ (c) $\delta = 0.5, t = 2.142$

Figure 10: Pressure fields surrounding the bubbles when developing jets near a solid wall(plane $x = 0$) with $\epsilon = 100, \gamma_w = 1.0$ and different buoyancy parameters. The green surfaces are the bubbles and the others represent the iso-pressure surfaces.

0.1 to 0.5, the pressure peak decrease significantly from 6 to 1.5. As a result, the jet speed also decreases from 5.8 to 2.3 while the width is getting greater. This phenomenon is attributed to the effective developing time of the jet. With a higher

buoyancy parameter, the jet develops earlier during the collapse of the bubble, which also leads to an earlier penetration time. As a result, the jet is not well developed and the speed is slower when it penetrates the bubble.

After the jet impact, the bubbles are penetrated and turn into toroidal. The evolution of the toroidal bubbles with $\delta = 0.25$ at $t = 2.308, 2.370, 2.442$ and 2.595 are shown in Fig. 11, respectively. It is found that the evolution process differs from

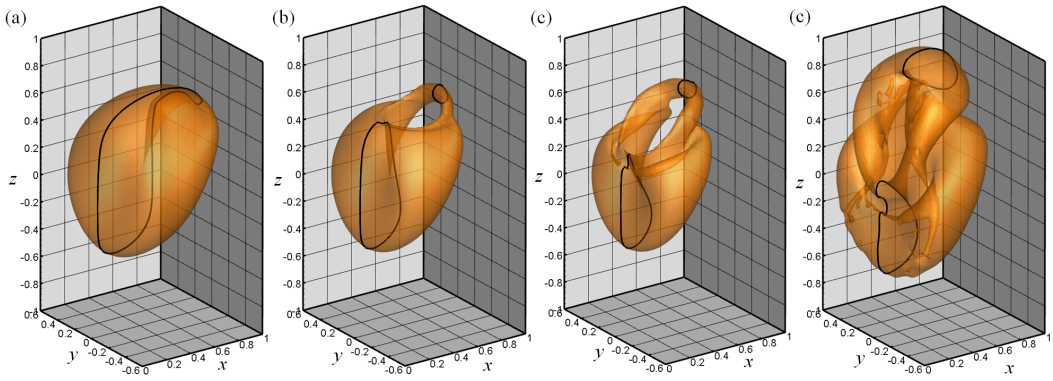

Figure 11: Toroidal bubble evolution beside a vertical solid wall(plane $x = 0$) with $\epsilon = 100, \delta = 0.25$ and $\gamma_w = 1.0$ at $t = 2.308, 2.370, 2.442$ and 2.595, respectively. The solid black curve represents the bubble surface profile at the xoz plane.

the case with $\delta = 0.5$ shown in the subsection.4.3 significantly. Compared with the previous case, the diameter of the jet cross-section on the xoz plane is much smaller such that the cross-section tends to be a circle rather than an ellipse-shape with smaller buoyancy effects. Thus, the part of the toroidal bubble close to the wall has the maximum cross-section along the toroid. It has been shown by Klaseboer et al. [20] that the direction of the liquid jet tilted upwards initially will shift more and more perpendicular to the solid wall, which was attributed to the growing attraction effect from the solid wall as the center of the bubble rushes to the wall. From the theoretical view, it can also be explained with the mirror theory. The effect of the solid wall on the toroidal bubble can be imitated by an imaginary mirrored bubble on the other side of the solid wall, as shown in Fig. 12. The velocity circulation caused by the imaginary bubble leads to a downward induced velocity around the real bubble. The induced velocity decays along with the distance from the imaginary bubble. Thus, the fluid flow around the real bubble tends to be rotated anticlockwise. As a result, the jet direction shifts to the solid wall, and the cross-section of the toroidal bubble close to the solid wall diminishes while the cross-section away from the wall is enlarged during the shift of the jet direction. This also explains why the toroidal

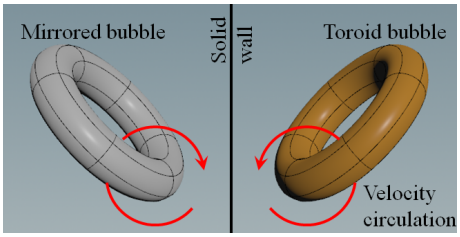

Figure 12: Sketch of the mirror theory of the toroidal bubble beside a solid wall.

bubble hardly breaks into a crescent-shape from the part away from the wall. Fig. 13 shows the pressure field on the solid wall generated by the toroidal bubble at the same times presented in Fig. 11. We can see that the pressure on the solid wall before the jet penetration only varies from 2 to 2.6, because the jet develops on the side of the bubble away from the solid wall. When the bubble is penetrated by the jet, a high-pressure region emerges around $[y, z] = [0, 0.8]$ where the jet is pointing. Because of the angle between the directions of the jet and the normal of the solid wall is quite large, the impact pressure is only 8 at this time and reaches 26 at $t = 2.442$ when the jet is fully developed. Then, the jet pressure drops to 5 as the bubble rebounds.

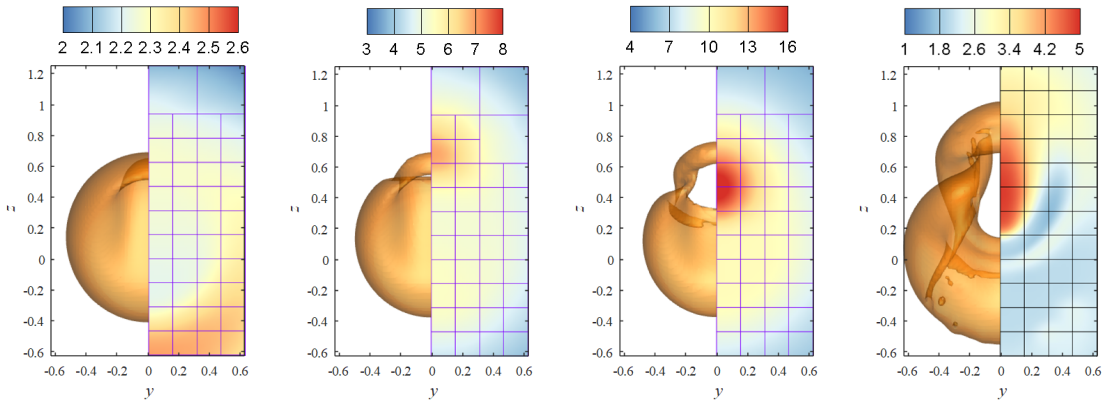

(a) $t = 2.308$ (b) $t = 2.370$ (c) $t = 2.442$ (d) $t = 2.595$

Figure 13: Pressure field on the vertical solid wall (plane $x = 0$) generated by the impact of a toroidal bubble with $\epsilon = 100, \delta = 0.25$ and $\gamma_w = 1.0$ at the same times shown in Fig. 11. The left sides are the bubble surface while the right sides are the corresponding pressure contours.

When the buoyancy parameter δ decreases to 0.1, the evolution of the toroidal bubble after the jet penetration is shown in Fig. 14. It can be seen that the attraction

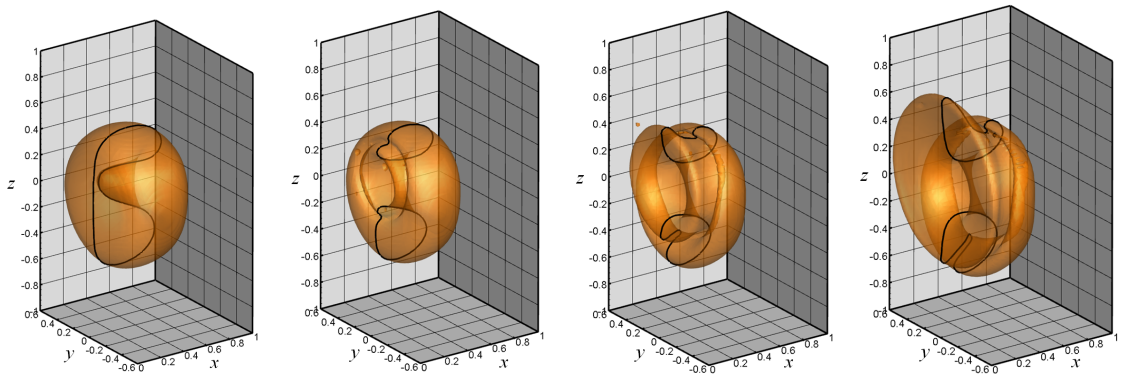

(a) $t = 2.342$ (b) $t = 2.397$ (c) $t = 2.462$ (d) $t = 2.530$

Figure 14: Toroidal bubble evolution beside a vertical solid wall (plane $x = 0$) with $\epsilon = 100, \delta = 0.1$ and $\gamma_w = 1.0$. The solid black curve represents the bubble surface profile at the xoz plane.

of the solid wall dominates the motion of the bubble while the buoyancy is so small that the direction of the jet is almost perpendicular to the solid wall with a little inclination upwards. Similar to the axisymmetrical problems presented by Tian et al. [40] and Wang et al. [45], the necking effect and the bubble volume transportation from the old toroidal bubble to the new one are observed. Fig. 15 shows the impact pressure on the solid wall caused by the collapsing bubble at the same times shown in Fig. 14. We can see that the impact pressure emerges even before the penetration at $t = 2.342$, which means that the gas layer between the jet tip and the opposite bubble surface can transmit great pressure when they are close enough to each other. This phenomenon is similar to the air cushion effect in the high-speed water entry problem. It violates the uniform pressure assumption of the internal gas used in the BEMs and gives more reliable results. The jet impact pressure rises quickly after the penetration and then decays with the rebound of the toroidal bubble.

To quantitatively compare the bubble loads caused by the jets with different buoyancy parameters, the pressure histories at the jet impact points on the solid wall are drawn together in Fig. 16. The bubble pulsating load decreases with the increase of the buoyancy parameter. The reason is that with a greater buoyancy parameter, the jet is better developed with a greater diameter and a higher speed at the same time. Thus, more energy of the system transfers to the surrounding fluid's kinetic energy, such that the residual energy to suppress the bubble and generate the pulsating load is less. This can be justified by comparing the minimum volumes of the bubbles, as shown in Tab. 2. The minimum volume of the bubble with $\delta = 0.5$ is the greatest among the 3 cases, and its pulsating pressure is the minimum. In the

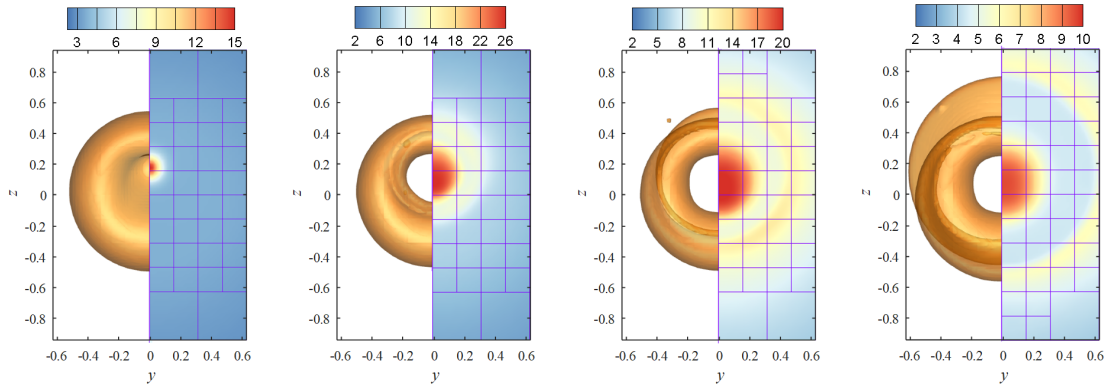

(a) $t = 2.342$ (b) $t = 2.397$ (c) $t = 2.462$ (d) $t = 2.530$

Figure 15: Pressure field on the vertical solid wall (plane $x = 0$) generated by the impact of a toroidal bubble with $\epsilon = 100, \delta = 0.1$ and $\gamma_w = 1.0$ at the same times shown in Fig. 14. The left sides are the bubble surface while the right sides are the corresponding pressure contours.

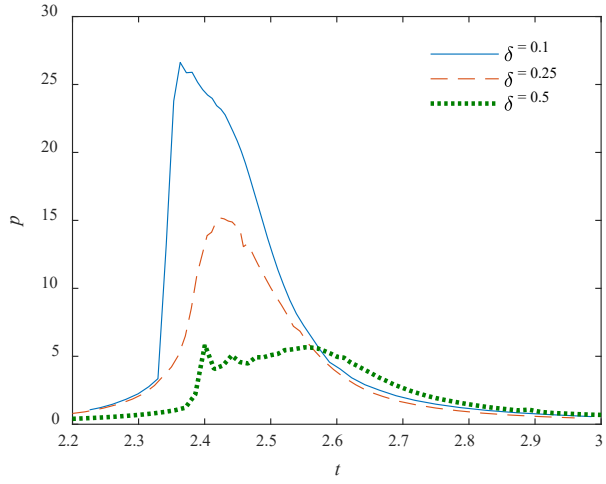

Figure 16: Comparison of jet impact pressure histories on the solid wall generated by the bubbles with $\delta = 0.1, 0.25$ and 0.5, respectively.

Table 2: Minimum volumes of the bubbles with different buoyancy parameters and the corresponding times

	$\delta = 0.1$	$\delta = 0.25$	$\delta = 0.5$
$v_{\min}$	0.177	0.192	0.298
time	2.449	2.475	0.256

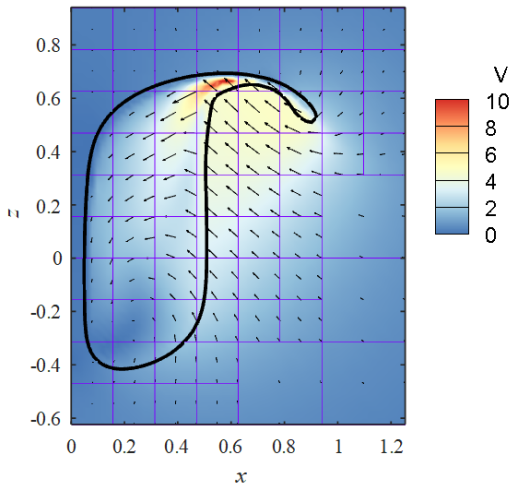

Figure 17: Velocity field of the plane $y = 0$ at $t = 2.308$ near the bubble with $\delta = 0.25$. The arrows indicate the velocity direction and the color contour represents the magnitude.

case with $\delta = 0.25$, the pressure history is relatively smooth, and no obvious sharp increase is observed, which indicates that the jet penetrates the bubble moderately. The velocity field at the moment of the jet penetration is shown in Fig. 17. It can be seen that the direction of the jet velocity is almost parallel to the opposite bubble surface at the first impact point. Thus, the relative velocity at the normal direction is small such that the penetration is a mild process. As for the case with the smallest buoyancy parameter $\delta = 0.1$, the pressure peak of the bubble load is almost twice of that with $\delta = 0.25$, although they have similar minimum volumes. It is attributed to the jet impact pressure on the solid wall. In this case, the jet has a higher speed and its direction is almost perpendicular to the opposite bubble surface such that the impact pressure is maximized.

5. Conclusions

In this paper, a 3-D numerical model based on the Eulerian FEM is established to investigate the bubble collapse near a solid wall. The block-based AMR technique is adopted to reduce the computational cost while maintaining the accuracy near the bubble. An experiment is carried out to validate the numerical model and the convergence of the present model is demonstrated by comparing the results with those obtained with the BEM. Through the simulation and the analysis of several cases with different buoyancy parameters, the following conclusions are drawn:

(1) Both the evolution of the single-connect bubble before the jet penetration and the multi-connect bubble are dominated by the joint effects of the buoyancy and the solid wall. Their balance determines the dynamic feature of the bubble and its hydrodynamic pressure on the solid wall;

(2) The direction of the tilted jet will shift towards the solid wall gradually during the collapse of the toroidal bubble after the jet penetration, which can be explained with the mirror theory and attributed to the velocity circulation caused by the imaginary toroidal bubble. The toroidal bubble may further break into a crescent-shape if the buoyancy is strong enough. The cross-section of the toroidal bubble is thinner at the part close to the solid wall due to the buoyancy such that the toroidal bubble breaks from here when the jet shifts downwards;

(3) The air cushion effect is observed between the jet tip and the opposite bubble surface before the jet impact, and it causes the solid wall to experience the impact pressure in advance of the penetration;

(4) The penetration of the bubble by the jet may generate an impact pressure on the nearby wall depending on the jet speed and direction. When the jet velocity is perpendicular to the opposite bubble surface, the impact pressure is maximized.

Acknowledgments

This work was supported by the National Natural Science Foundation of China (grant numbers 51879050 and 52088102), the China Postdoctoral Science Foundation (grant numbers 2016M600244 and 2018T110271), and the Heilongjiang Postdoctoral Fund (grant numbers LBH-Z20131, LBH-TZ07). The authors would like to acknowledge Doc. Nian-Nian Liu for the help in implementing the experiment.

The Paramesh used in this work was developed at the NASA Goddard Space Flight Center and Drexel University under NASA's HPCC and ESTO/CT projects and under grant NNG04GP79G from the NASA/AISR project.

References

[1] G. Barras, M. Souli, N. Aquelet, and N. Couty. Numerical simulation of underwater explosion using an ale method. *Ocean Engineering*, 41:53–66, 2012.

[2] D. J. Benson. Momentum advection on a staggered mesh. *Journal of Computational Physics*, 100(1):143–162, 1992.

[3] D. J. Benson. Computational methods in Lagrangian and Eulerian hydrocodes. *Computer Methods in Applied Mechanics and Engineering*, 99(2):235–394, 1992.

[4] M.J. Berger and P. Colella. Local adaptive mesh refinement for shock hydrodynamics. *Journal of Computational Physics*, 82(1):64 – 84, 1989.

[5] J. R. Blake, B. B. Taib, and G. Doherty. Transient cavities near boundaries. part 1. rigid boundary. *Journal of Fluid Mechanics*, 170:479–497, 1986.

[6] C. Brennen. *Cavitation and Bubble Dynamics*, volume 44 of *Cavitation and Bubble Dynamics*. Oxford University Press, Oxford, 1995.

[7] E.-A. Brujan, T. Noda, A. Ishigami, T. Ogasawara, and H. Takahira. Dynamics of laser-induced cavitation bubbles near two perpendicular rigid walls. *Journal of Fluid Mechanics*, 841:28–49, 2018.

[8] G. L. Chahine, A. Kapahi, J.-K. Choi, and C.-T. Hsiao. Modeling of surface cleaning by cavitation bubble dynamics and collapse. *Ultrasonics Sonochemistry*, 29:528–549, 2016.

[9] G. L. Chahine, A. Gnanaskandan, A. Mansouri, C.-T. Hsiao, and R. Content. Interaction of a cavitation bubble with a polymeric coating–scaling fluid and material dynamics. *International Journal of Multiphase Flow*, 112:155–169, 2019.

[10] S. Chelminski, L. M. Watson, and S. Ronen. Research note: Low-frequency pneumatic seismic sources. *Geophysical Prospecting*, 67(6):1547–1556, 2019.

[11] J. Cheng, F. Zhang, and T. Liu. A discontinuous galerkin method for the simulation of compressible gas-gas and gas-water two-medium flows. *Journal of Computational Physics*, 403:109059, 2020.

[12] R. H. Cole. *Underwater explosion*. Princeton University Press, Princeton, USA, 1948.

[13] J. Cui, Z.-P. Chen, Q. Wang, T.-R. Zhou, and C. Corbett. Experimental studies of bubble dynamics inside a corner. *Ultrasonics Sonochemistry*, 64:104951, 2020.

[14] A. Daramizadeh and M.R. Ansari. Numerical simulation of underwater explosion near air–water free surface using a five-equation reduced model. *Ocean Engineering*, 110:25 – 35, 2015.

[15] B. Dollet, P. Marmottant, and V. Garbin. Bubble dynamics in soft and biological matter. *Annual Review of Fluid Mechanics*, 51(1):331–355, 2019.

[16] R. P. Fedkiw, T. Aslam, B. Merriman, and S. Osher. A non-oscillatory Eulerian approach to interfaces in multimaterial flows(the Ghost Fluid Method). *Journal of Computational Physics*, 152:457–492, 1999.

[17] C. W. Hirt and B. D. Nichols. Volume of fluid method for the dynamics of free boundaries. *Journal of Computational Physics*, 39:201–225, 1981.

[18] M. J. Ivings, D. M. Causon, and E. F. Toro. On riemann solvers for compressible liquids. *International Journal for Numerical Methods in Fluids*, 28(3):395–418, 1998.

[19] E. Johnsen and T. I. M. Colonius. Numerical simulations of non-spherical bubble collapse. *Journal of Fluid Mechanics*, 629:231–262, 2009.

[20] E. Klaseboer, K. C. Hung, C. W. Wang, and B. C. Khoo. Experimental and numerical investigation of the dynamics of an underwater explosion bubble near a resilient/rigid structure. *Journal of Fluid Mechanics*, 53(7):387–413, 2005.

[21] E. Klaseboer, C. Turangan, S. W. Fong, T. G. Liu, K. C. Hung, and B. C. Khoo. Simulations of pressure pulse–bubble interaction using boundary element method. *Computer Methods in Applied Mechanics and Engineering*, 195(33): 4287 – 4302, 2006.

[22] M. Kornfeld and L. Suvorov. On the destructive action of cavitation. *Journal of Applied Physics*, 15(6):495–506, 1944.

[23] S. Li, D. Meer, A.-M. Zhang, A. Prosperetti, and D. Lohse. Modelling large scale airgun-bubble dynamics with highly non-spherical features. *International Journal of Multiphase Flow*, 122:103143, 01 2020.

[24] T. G. Liu, B. C. Khoo, and K. S. Yeo. Ghost fluid method for strong shock impacting on material interface. *Journal of Computational Physics*, 190:651–681, 2003.

[25] Y. Liu, A.-M. Zhang, Z. Tian, and S. Wang. Investigation of free-field underwater explosion with Eulerian finite element method. *Ocean Engineering*, 166: 182–190, 2018.

[26] Y.-L. Liu, A.-M. Zhang, Z.-L. Tian, and S.-P. Wang. Dynamical behavior of an oscillating bubble initially between two liquids. *Physics of Fluids*, 31(9):092111, 2019.

[27] Y.-L. Liu, S. Chi-Wang, and Z. A-Man. Weighted ghost fluid discontinuous galerkin method for two-medium problems. *Journal of Computational Physics*, 426:109956, 2021.

[28] Y.L. Liu, Q.X. Wang, S.P. Wang, and A.M. Zhang. The motion of a 3d toroidal bubble and its interaction with a free surface near an inclined boundary. *Physics of Fluids*, 28(12):122101, 2016.

[29] P. MacNeice, K. M. Olson, C. Mobarry, R. de Fainchtein, and C. Packer. Paramesh: A parallel adaptive mesh refinement community toolkit. *Computer Physics Communications*, 126(3):330–354, 2000.

[30] P. MacNeice, K. M. Olson, C. Mobarry, R. de Fainchtein, and C. Packer. Paramesh: A parallel adaptive mesh refinement community toolkit. *Computer Physics Communications*, 126(3):330–354, 2000.

[31] A. Murrone and H. Guillard. A five equation reduced model for compressible two phase flow problems. *Journal of Computational Physics*, 202(2):664 – 698, 2005.

[32] C. F. Naude. *On the mechanism of cavitation damage by non-hemispherical cavities collapsing in contact with a solid boundary.* Thesis, 1960.

[33] K. Olson. *PARAMESH: A Parallel, Adaptive Grid Tool*, pages 341–348. Elsevier, Amsterdam, 2006.

[34] K. M. Olson and P. MacNeice. An overview of the paramesh amr software package and some of its applications. In T. Plewa, T. Linde, and V. Gregory Weirs, editors, *Adaptive Mesh Refinement - Theory and Applications*, pages 315–330, Berlin, Heidelberg, 2005. Springer Berlin Heidelberg.

[35] M.S. Plesset and R.B. Chapman. Collapse of an initially spherical vapor cavity in the neighborhood of a solid boundary. *Journal of Fluid Mechanics*, 47:283–290, 1971.

[36] A. Prosperetti and A. Lezzi. Bubble dynamics in a compressible liquid. part 1. first-order theory. *Journal of Fluid Mechanics*, 168:457–478, 1986.

[37] L. Rayleigh. Viii. on the pressure developed in a liquid during the collapse of a spherical cavity. *Philosophical Magazine and Journal of Science*, 34(200):94–98, 1917.

[38] K. K. So, X. Y. Hu, and N. A. Adams. Anti-diffusion interface sharpening technique for two-phase compressible flow simulations. *Journal of Computational Physics*, 231:4304–4323, 2012.

[39] Z.-L. Tian, Y.-L. Liu, A.-M. Zhang, and L. Tao. Energy dissipation of pulsating bubbles in compressible fluids using the eulerian finite-element method. *Ocean Engineering*, 196:106714, 2020.

[40] Z.-L. Tian, Y.-L. Liu, A.-M. Zhang, L. Tao, and L. Chen. Jet development and impact load of underwater explosion bubble on solid wall. *Applied Ocean Research*, 95:102013, 2020.

[41] C. Wang and C.-W. Shu. An interface treating technique for compressible multi-medium flow with runge–kutta discontinuous galerkin method. *Journal of Computational Physics*, 229(23):8823–8843, 2010.

[42] C. Wang and C.-W. Shu. An interface treating technique for compressible multi-medium flow with Runge-Kutta discontinuous Galerkin method. *Journal of Computational Physics*, 229:8823–8843, 2010.

[43] Q. Wang. Multi-oscillations of a bubble in a compressible liquid near a rigid boundary. *Journal of Fluid Mechanics*, 745:509–536, Apr 2014.

[44] Q. X. Wang. The evolution of a gas bubble near an inclined wall. *Theoretical and Computational Fluid Dynamics*, 12(1):29–51, 1998. ISSN 1432-2250.

[45] Q. X. Wang, K. S. Yeo, B. C. Khoo, and K. Y. Lam. Vortex ring modelling of toroidal bubbles. *Theoretical & Computational Fluid Dynamics*, 19(5):303–317, 2005.

[46] S.-P. Wang, A.-M. Zhang, Y.-L. Liu, S. Zhang, and P. Cui. Bubble dynamics and its applications. *Journal of Hydrodynamics*, 30(6):975–991, 2018.

[47] S. R. Wu and L. Gu. *Introduction to the explicit finite element method for nonlinear transient dynamics*. John Wiley & Sons, Inc., Hoboken, USA, 2012.

[48] T. Ye, W. Shyy, and J. N. Chung. A fixed-grid, sharp-interface method for bubble dynamics and phase change. *Journal of Computational Physics*, 174(2): 781 – 815, 2001.

[49] D. L. Youngs. *Numerical Methods in Fluid Dynamics*. Academic Press, New York, 1982.

[50] A. M. Zhang and Y. L. Liu. Improved three-dimensional bubble dynamics model based on boundary element method. *Journal of Computational Physics*, 294: 208–223, 2015.

[51] A. M. Zhang, S. Li, and J. Cui. Study on splitting of a toroidal bubble near a rigid boundary. *Physics of Fluids*, 27(6):062102, 2015.

[52] S. Zhang, S.-P. Wang, Y.-L. Liu, A.-M. Zhang, and P. Cui. Interaction of clustered air gun bubbles in marine prospecting. *Ocean Engineering*, 191:106523, 2019.